ADVANCED FUNCTIONAL MATERIALS
www.afm-journal.de

Removing Homocoupling Defects in Alkoxy/Alkyl-PBTTT Enhances Polymer:Fullerene Co-Crystal Formation and Stability

Zhen Liu, Jochen Vanderspikken, Paola Mantegazza, Stefania Moro, Mouna Hamid, Sigurd Mertens, Niko Van den Brande, Laurence Lutsen, Vincent Lemaur, David Beljonne, Giovanni Costantini, Koen Vandewal,* Bruno Van Mele, Wouter Maes, and Bart Goderis**

C_{14}-alkoxy/alkyl PBTTT-OR-R, a derivative of the prototype PBTTT polymer, is relevant for optoelectronic applications because it combines PBTTT-like intercalation behavior with enhanced charge-transfer absorption at longer wavelengths. Additionally, fundamental insights are achieved by comparing this alternating conjugated polymer in the presence and absence of homocoupling defects. While the homocoupling-free oxidative variant, PBTTT-OR-R(O), as well as the Stille polymer with 19% homocoupling defects, PBTTT-OR-R(S), can both form co-crystals when stoichiometrically mixed with $PC_{61}BM$, the co-crystal of the latter shows properties which are highly dependent on the thermal processing conditions because of the presence of these defects. The PBTTT-OR-R(S):$PC_{61}BM$ co-crystal shows a low thermal stability and $PC_{61}BM$ can progressively be expelled upon heating. In cooling from the melt and depending on the cooling rate, mixtures of PBTTT-OR-R(S) and $PC_{61}BM$ show a competition between *co-crystallization* (fast cooling) and *separate crystallization* (slow cooling). The PBTTT-OR-R(O):$PC_{61}BM$ co-crystal is much more stable up to at least 260 °C and is not influenced by the applied cooling rate. These findings also translate to the device level. The performance of PBTTT-OR-R:$PC_{61}BM$ photodiodes is severely deteriorated after isothermal annealing in case of PBTTT-OR-R(S), whereas the thermally robust co-crystals of PBTTT-OR-R(O) allow a more flexible design of optimized devices.

1. Introduction

Semiconducting conjugated polymers[1] are prevailing materials in bulk heterojunction (BHJ) active layers for organic electronics applications such as organic solar cells (OSCs)[2,3] and organic photodetectors (OPDs).[4] In such excitonic BHJ devices, most often, electron-donating conjugated polymers are intimately mixed with electron-accepting small molecules or polymers to efficiently generate free charges from the coulombically bound electron-hole pairs created upon light absorption.[2] Modification of the polymer's chemical structure permits tuning of optoelectronic properties like absorption, frontier molecular orbital energies, and charge transport, and physical characteristics such as solubility, flexibility, (semi)crystallinity, and miscibility with the acceptor component.[1,5]

State-of-the-art conjugated polymers, push-pull (or donor–acceptor) alternating copolymers in particular,[6,7] show excellent tunability and satisfactory semiconducting

Z. Liu[+], N. Van den Brande, B. Van Mele
Lab of Physical Chemistry and Polymer Science (FYSC)
Research group Sustainable Materials Engineering (SUME)
Vrije Universiteit Brussel (VUB)
Pleinlaan 2, Brussels B-1050, Belgium
E-mail: liuzhen@opt.ac.cn

The ORCID identification number(s) for the author(s) of this article can be found under https://doi.org/10.1002/adfm.202413647

[+]Present address: Key Laboratory of Transient Optics and Photonics, Xi'an Institute of Optics and Precision Mechanics (XIOPM), Chinese Academy of Sciences (CAS), Information road 17, Xi'an, Shaanxi 710119, China

DOI: 10.1002/adfm.202413647

J. Vanderspikken, S. Mertens, K. Vandewal, W. Maes
Institute for Materials Research (imo-imomec)
Hasselt University
Martelarenlaan 42, Hasselt B-3500, Belgium
E-mail: koen.vandewal@uhasselt.be

J. Vanderspikken, S. Mertens, L. Lutsen, K. Vandewal, W. Maes
imec, imo-imomec
Wetenschapspark 1, Diepenbeek B-3590, Belgium

J. Vanderspikken, L. Lutsen
Energyville
imo-imomec
Thor Park 8320, Genk B-3600, Belgium

P. Mantegazza, S. Moro, G. Costantini
School of Chemistry
University of Birmingham
Birmingham, Edgbaston B15 2TT, United Kingdom

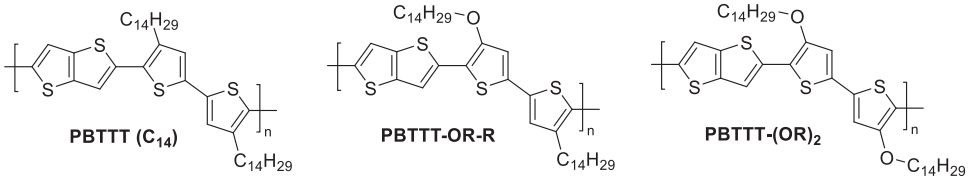

Figure 1. Chemical structure of PBTTT (C_{14}) and its alkoxy variants PBTTT-OR-R and PBTTT-$(OR)_2$.

properties. As such, they are competitive alternatives to inorganic semiconductors for specific applications.[8] These push–pull copolymers are generally synthesized by transition metal catalyzed Stille, Suzuki, or direct arylation cross-coupling polymerization methods which, in theory, should produce a perfect alternation of the two (push and pull) building blocks throughout the polymer backbone.[7,9–11] However, side reactions do occur producing, for instance, homocoupling sequences along the polymer chain,[9] wherein the building blocks have reacted with themselves rather than the complementary functionalized monomer. These homocoupling structural defects become an integral part of the polymer chains and cannot simply be removed, and have been shown to negatively affect OSC performance.[9,12–15] Although the occurrence of these defects during polymer synthesis is a well-known issue, the detailed impact of homocouplings on optoelectronic properties such as charge transport as well as the intimate interactions with the electron acceptor counterparts remains unclear. In fact, the presence of these structural defects is often simply ignored because they are deemed negligible or unavoidable, homocoupling-free polymers are not readily available, and an accurate quantification of the defect ratio is not at all straightforward using conventional techniques such as NMR spectroscopy.[9]

In previous work, we have shown that derivatives of the benchmark conjugated polymer PBTTT (poly[2,5-bis(3-tetradecylthiophen-2-yl)thieno[3,2-*b*]thiophene;[16] **Figure 1**) are excellent model systems to study the effect of homocoupling on polymer and blend properties.[17] Although PBTTT is, strictly speaking, not a strong push-pull copolymer and only affords moderate OSC efficiencies, it is semi-crystalline and shows a reasonably high hole mobility.[16,18] As such, it remains an important prototypical system for fundamental (e.g., doping)[19–22] studies as well as a state-of-the-art material for specific optoelectronic applications.[23,24] For instance, PBTTT:$PC_{61}BM$ ([6,6]-phenyl-C_{61}-butyric acid methyl ester) is a reference combination for cavity-based wavelength-selective near-infrared (NIR) OPDs that utilize the direct charge-transfer (CT) absorption for efficient narrow-band photodetection beyond the regime of conventional silicon PDs.[25,26] This is related to the fact that PBTTT uniquely forms co-crystals when mixed with fullerene derivatives by intercalating the "buckyballs" between its side chains,[27–29] affording a maximized donor:acceptor interface which promotes direct CT absorption.

When replacing the alkyl side chains of PBTTT by alkoxy substituents, hereby raising the energy of the highest occupied molecular orbital (HOMO), the CT absorption of the polymer:$PC_{61}BM$ blend shows a bathochromic shift.[4] If only one half of the side chains are altered to obtain PBTTT-OR-R (Figure 1), the unique fullerene intercalation features of PBTTT, the large donor:acceptor interfacial area, and the relatively strong CT absorption are maintained.[30] Incorporation into a microcavity device hence afforded narrow-band OPDs (i.e., full-width-at-half-maximum down to 30 nm) with specific detectivities up to 5×10^{11} Jones between 1000 and 1340 nm.[4] On the other hand, when all side chains were changed for alkoxy variants, the resulting PBTTT-$(OR)_2$ polymer (Figure 1) was – despite its further red-shifted CT absorption – not very effective in cavity OPDs, which was attributed to the less efficient fullerene intercalation (as evidenced by the reduced external quantum efficiency (EQE) in the CT range and preliminary thermal analysis and X-ray diffraction (XRD) experiments).[30]

In follow-up work, it was shown that the PBTTT-$(OR)_2$ polymer as synthesized by the traditional Stille cross-coupling in fact contained a significant amount (26%) of homocoupling defects.[17] A (virtually) defect-free variant was then synthesized via a conceptually simple, yet efficient symmetric oxidative polymerization approach. Comparison of the polymer samples with and without homocoupling by rapid heat-cool differential scanning calorimetry (RHC) and temperature-resolved synchrotron XRD indicated that PBTTT-$(OR)_2$ can only form co-crystals with $PC_{61}BM$ when the homocoupling defects are removed. Consequently, the CT absorption – of which the strength strongly relies on the large interface such co-crystals provide – was promoted for homocoupling-free PBTTT-$(OR)_2$.[17]

In the present study, we extend this approach to the previously most promising PBTTT-OR-R derivative. We accurately determine the amount of defects in Stille polymerized PBTTT-OR-R, present an optimized synthetic protocol to obtain a homocoupling-free variant, and use PBTTT-OR-R:$PC_{61}BM$ as a model system to investigate the influence of homocoupling defects on thermal, morphological, and device properties. By combining matrix-assisted laser desorption/ionization – time of flight mass spectrometry (MALDI-ToF MS) and a quantitative analysis of ultrahigh vacuum scanning tunneling microscopy (UHV-STM) images, it is demonstrated that also the Stille PBTTT-OR-R contains a large amount of homocoupled units (19%), whereas the oxidative variant is almost defect-free. The thermal properties and temperature-dependent morphology of Stille PBTTT-OR-R and its oxidative variant (henceforth labeled as (S) and

M. Hamid, B. Goderis
Polymer Chemistry and Materials Division
KU Leuven
Celestijnenlaan 200F, Heverlee B-3001, Belgium
E-mail: bart.goderis@kuleuven.be
V. Lemaur, D. Beljonne
Laboratory for Chemistry of Novel Materials
Materials Research Institute
University of Mons (UMONS)
20 Place du Parc, Mons B-7000, Belgium

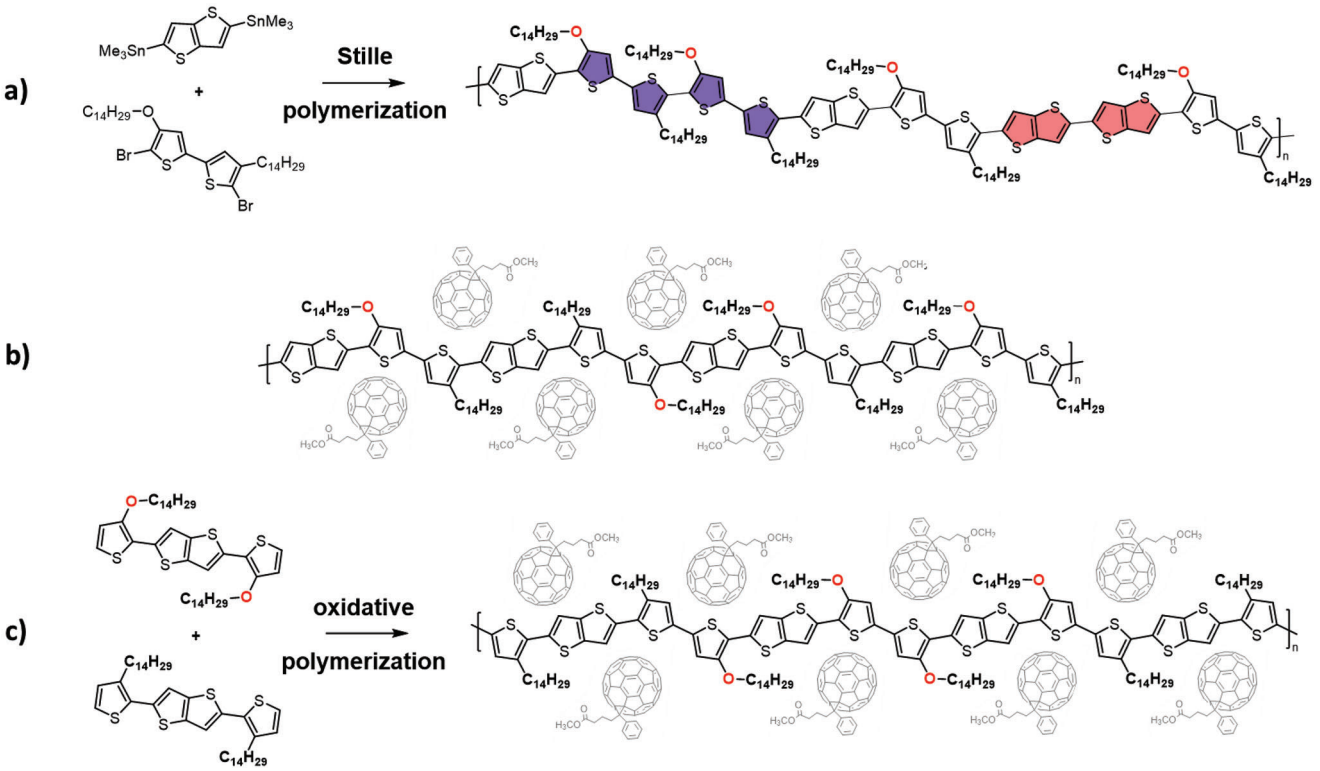

Figure 2. Overview of a) the Stille cross-coupling approach for PBTTT-OR-R, with visualization of TT (red) and BT (purple) homocouplings, b) the concomitant regiochemical irregularities and different "docking" sites for $PC_{61}BM$ (even when neglecting homocoupling), and c) the oxidative polymerization strategy, avoiding homocoupling but still affording some degree of irregularity in the side chain positioning.

(O), respectively) are compared as pristine materials and in mixtures with $PC_{61}BM$ by a combination of RHC, temperature-resolved synchrotron XRD, and molecular dynamics (MD) simulations. Although PBTTT-OR-R(O) and PBTTT-OR-R(S) can both form co-crystals when stoichiometrically mixed with $PC_{61}BM$, the PBTTT-OR-R(S):$PC_{61}BM$ co-crystals show a much lower thermal stability. Importantly, these observations also translate to the device level. EQE spectra for polymer:fullerene BHJ photodiodes after thermal annealing confirm that device performance is severely deteriorated in case of PBTTT-OR-R(S), leading to less reliable and reproducible devices, illustrating the crucial importance of defect-free synthesis for the envisaged optoelectronic applications.

2. Results and Discussion

2.1. Polymer Synthesis and Structural Characterization

In this work, two samples of the mixed (50/50) alkoxy/alkyl-PBTTT-OR-R polymer are compared, synthesized either via the Stille or the oxidative polymerization method. The Stille cross-coupling for PBTTT-OR-R implies the reaction of an asymmetrically substituted, dibrominated bithiophene monomer with 2,5-bis(trimethylstannyl)thieno[3,2-*b*]thiophene (**Figure 2a**).[30] However, as mentioned above, this reaction might also afford bithiophene (BT) and thienothiophene (TT) homocouplings (highlighted in purple and red, respectively, in Figure 2a). Additionally, and different from PBTTT and the fully alkoxylated PBTTT-$(OR)_2$, the PBTTT-OR-R(S) polymer is irregular with respect to the placement of the side chains. Although each BT unit always contains one alkyl and one alkoxy substituent, the BT monomers are randomly oriented throughout the polymer chain, which gives rise to different "docking" environments for the fullerene molecules (Figure 2b), even when not considering homocoupling.

For the oxidative approach toward PBTTT-OR-R, it was opted to combine the symmetrical 2,5-bis(3-tetradecylthiophen-2-yl)thieno[3,2-*b*]thiophene and 2,5-bis(3-(tetradecyloxy)thiophen-2-yl)thieno[3,2-*b*]thiophene monomers in an equimolar ratio and react them in the presence of iron(III) chloride (Figure 2c).[17] This inherently avoids homocoupling defects but the individual polymer chains can contain varying ratios of alkyl and alkoxy side chains, with potentially longer sequences of the same substituents. Similar side chain stereo-irregularities as for the Stille case are expected to occur also here. The synthesis of the two monomers and the oxidative polymerization method are outlined in detail in the Supporting Information (NMR spectra in Figures S1–S3, Supporting Information), whereas synthesis and characterization data for PBTTT-OR-R(S) were reported before.[30] It is important to note that all polymers were purified by repetitive Soxhlet extractions, as generally performed for conjugated polymers,[31] which implies that the isolated materials do not fully reflect the crude polymer mixture and specific oligomer and/or polymer chains might have been removed via the extraction solvents. Table S1 (Supporting Information) summarizes the main characteristics of the two polymers after Soxhlet purification. Gel

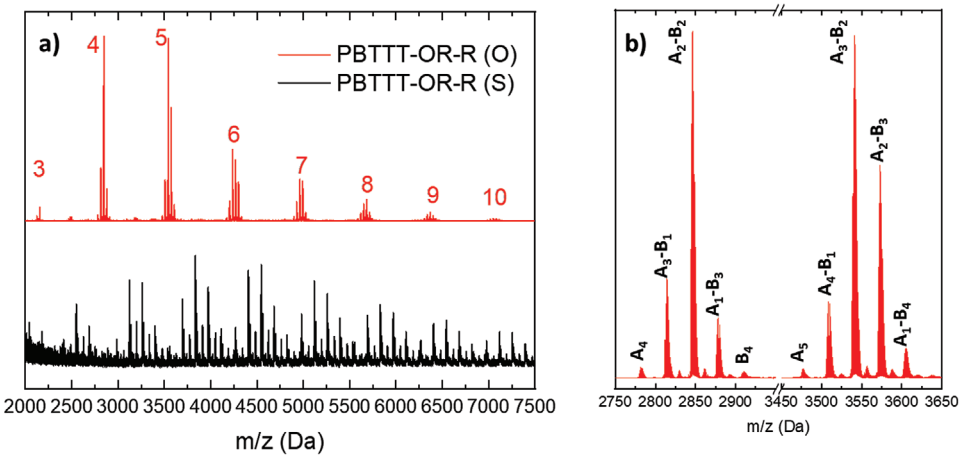

Figure 3. a) MALDI-ToF mass spectra (*m/z* range from 2000 to 7500 Dalton) of PBTTT-OR-R(O) (red) and PBTTT-OR-R(S) (black). The peak labels refer to the number of repeating units. b) Zoom-in onto the mass ranges corresponding to species with 4 and 5 repeating units for PBTTT-OR-R(O). The signal multiplicity is evident, due to the variation of alkyl and alkoxy side chains in the different polymer species. The label A corresponds to the alkylated and B to the alkoxylated symmetric monomer, respectively.

permeation chromatography (GPC) measurements indicate that PBTTT-OR-R(O) has a somewhat lower molar mass (number-average molar mass (M_n) of 24.4 kg mol^{-1}, versus 44.5 kg mol^{-1} for PBTTT-OR-R(S)). The ^{1}H NMR spectrum of PBTTT-OR-R(O) confirms that the copolymer chains on average contain an approximate 1:1 ratio of alkyl and alkoxy side chains (based on the integration of the methylene protons closest to the polymer backbone; Figure S3, Supporting Information). PBTTT-OR-R(O) and PBTTT-OR-R(S) display similar absorption spectra and frontier molecular orbital energy levels (as derived from cyclic voltammetry analysis) (Figures S4 and S5, Supporting Information), so possible homocouplings do not seem to influence these bulk properties to a large extent.

To assess the occurrence of homocoupling in the two polymer samples, we first turned to mass spectrometry. MALDI-ToF MS combines a low fragmentation tendency with a wide mass window and is hence particularly suited for polymer analysis. If a polymer is structurally pure, one expects to only see masses corresponding to N times the mass of the repeating unit. Furthermore, end-capped polymers or chains with incorrect ratios of monomers, which are distinctly different in mass, lead to additional and readily identifiable signals. When comparing the MALDI-ToF MS spectra of PBTTT-OR-R(S) and PBTTT-OR-R(O), it is clear that many fewer species are formed using the oxidative approach (**Figure** 3a). Indeed, the spectrum for PBTTT-OR-R(O) almost exclusively contains signals corresponding to multiples of the mass of the monomer repeating unit. The higher "multiplicity" of the signals for PBTTT-OR-R(O) reflects the copolymerization procedure and the presence of chains with different relative amounts of alkyl and alkoxy side chains. In Figure 3b, the signals for the species with 4 and 5 repeating units are shown in more detail and labeled with the corresponding composition, with A representing the alkylated and B the alkoxylated monomer, respectively. The bias toward more alkyl than alkoxy side chains, which contrasts the overall 1:1 ratio as indicated by NMR (Figure S3, Supporting Information), might have different origins. It is in fact important to stress that MALDI-ToF MS intensities cannot be treated quantitatively, i.e., they do not necessarily reflect the correct molar ratio of different species present within a polymer sample as they depend on the measurement conditions applied (e.g., the concentration of the analyte in the matrix and the laser power).[32]

On the other hand, the spectrum for PBTTT-OR-R(S) suggests the presence of (extensive) homocoupling, especially from the TT monomer (Figure S6, Supporting Information). A similar observation was previously made for PBTTT-(OR)$_2$,[17] where the excess of homocoupled over regular polymer chains seemed even more dramatic when relying on MALDI-ToF MS data. Nevertheless, STM analysis for the Stille-synthesized PBTTT-(OR)$_2$ sample indicated that both homocouplings (i.e., BT and TT) were present in similar amounts.[17] To achieve a reliable and quantitative evaluation of the polymerization defects, an analogous STM analysis was performed for both PBTTT-OR-R(S) and PBTTT-OR-R(O).[17,33–35]

Typical close-up STM images of these polymers, after electrospray deposition (ESD) onto an atomically clean Au(111)/mica surface, are shown in **Figure** 4a (PBTTT-OR-R(O)) and Figure 4b (PBTTT-OR-R(S)). The assembly pattern and molecular conformation of these two polymers are similar (see also Figures S7 and S8, Supporting Information) but fitting high-resolution images with MD-optimized molecular models reveals a substantial difference in the structure of their backbones. This fitting procedure (detailed in ref. [17]) enables the precise determination of the backbone sequence and the identification of any polymerization defects.

Three different types of polymerization defects were identified in PBTTT-OR-R(S) (Figure 4c), examples of which are shown in Figures 4e,f,g. The relative frequencies of these defects were obtained by fitting a statistically significant number of images and normalized by the total number of bonds counted between TT and BT units. The results of this analysis are displayed in the table in Figure 4h. It should be noted that similarly to what was observed for the Stille-synthesized PBTTT-(OR)$_2$,[17] the relative percentages of the two polymer subunits in PBTTT-OR-R(S)

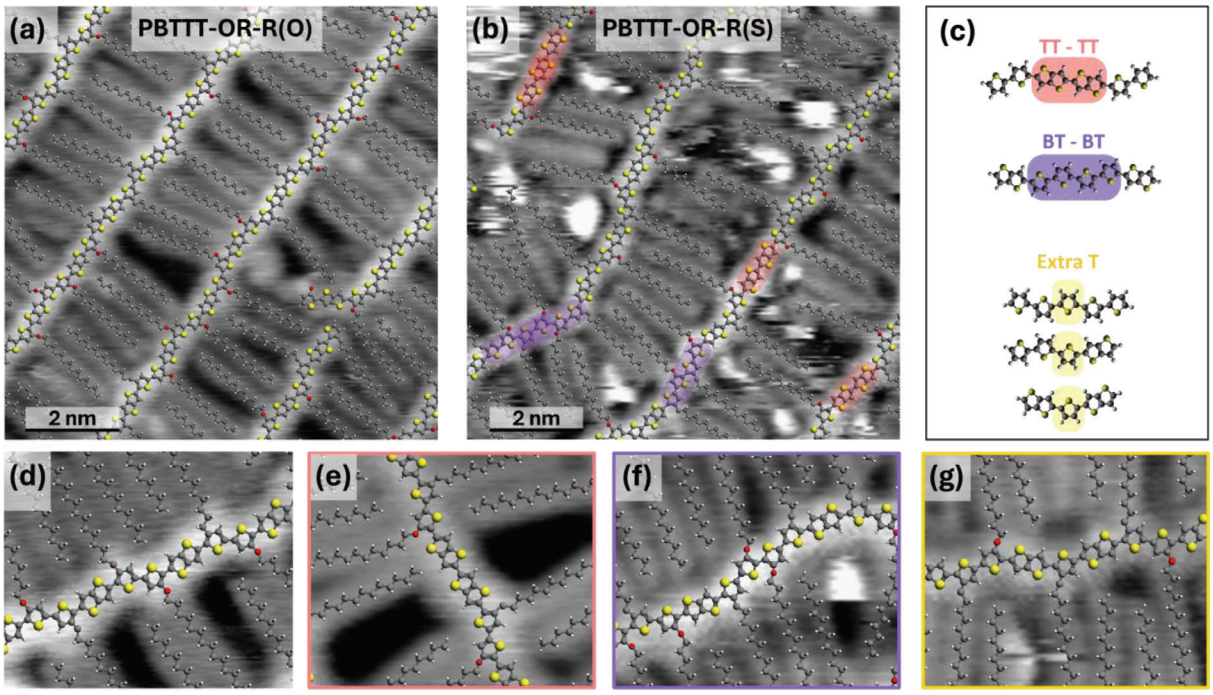

(h)	TT - TT	BT - BT	Extra T	BT - TT	Tot defects	Tot bonds	TT	BT	Tot monomers
bonds	89	111	6	859	206	1065	554	565	1119
%	8.3	10.4	0.6	80.7	19.3	100.0	49.5	50.5	100.0

Figure 4. a) High-resolution STM image of self-assembled PBTTT-OR-R(O), and b) PBTTT-OR-R(S) with the corresponding molecular models superimposed. c) Types of polymerization defects considered for fitting the STM images: TT and BT homocoupling, and the three possible cases of sequences with a single extra T. Zoomed-in details displaying d) the expected, defect-free alternating BT-TT sequence, e) TT homocoupling, f) BT homocoupling, and g) extra T defect. h) Frequencies of polymerization defects and monomers observed in PBTTT-OR-R(S). The frequencies of the defects were normalized by the total number of bonds between TT and BT units, and the monomers frequencies by the total number of TT and BT units.

are very similar (49.5% TT and 50.5% BT), indicating a possible overestimation of TT homocoupling by MALDI-ToF MS. When conducting the same type of analysis on high-resolution STM images of PBTTT-OR-R(O), virtually no defects were detected, with only a single TT homocoupling observed out of 698 counted bonds. For this polymer as well, the TT and BT subunits appear in almost identical relative frequencies, 50.3% and 49.7%, respectively.

Although smaller than the 26% defects observed in PBTTT-$(OR)_2$,[17] the overall fraction of 19% homocouplings observed in PBTTT-OR-R(S) is still surprisingly high, especially considering that the fullerene intercalation features were retained for this polymer.[30]

2.2. Polymer Morphology and Co-Crystal Formation

The impact of the presence of homocoupling defects on fullerene intercalation and on the temperature-dependent morphology and corresponding thermal properties of the pristine polymers and co-crystals was then analyzed in detail.

2.2.1. Thermal Analysis (RHC) of Polymers and Co-Crystals

The RHC thermograms of PBTTT-OR-R(O) and PBTTT-OR-R(S) in heating at 500 K min^{-1} after cooling from 320 °C at different cooling rates (from 5 to 500 K min^{-1}) are shown in **Figure 5**a,b, respectively, in comparison with their respective mixtures with $PC_{61}BM$ in 45:55 and 40:60 w/w% ratios, which are close to the 1:1 molar ratio (43:57 w/w%) of the polymer repeating unit and $PC_{61}BM$.

With increasing temperature, different thermal transitions occur depending on the absence or presence of $PC_{61}BM$ and the origin of PBTTT-OR-R (oxidative or Stille): i) alkoxy/alkyl (C_{14}) side chain melting around (PBTTT-OR-R(O)) and below 50 °C (PBTTT-OR-R(S)), indicative of the presence of a pure PBTTT-OR-R phase, as seen for instance for the pristine polymers. Side chain melting in the pristine polymers leads to a sanidic liquid crystalline state,[36] of which the structure is explained in the section dealing with the temperature-resolved XRD data (vide infra). The PBTTT-OR-R(O):$PC_{61}BM$ mixtures show no OR-R side chain melting at all, whereas the PBTTT-OR-R(S):$PC_{61}BM$ mixtures show a minor amount of side chain melting, especially

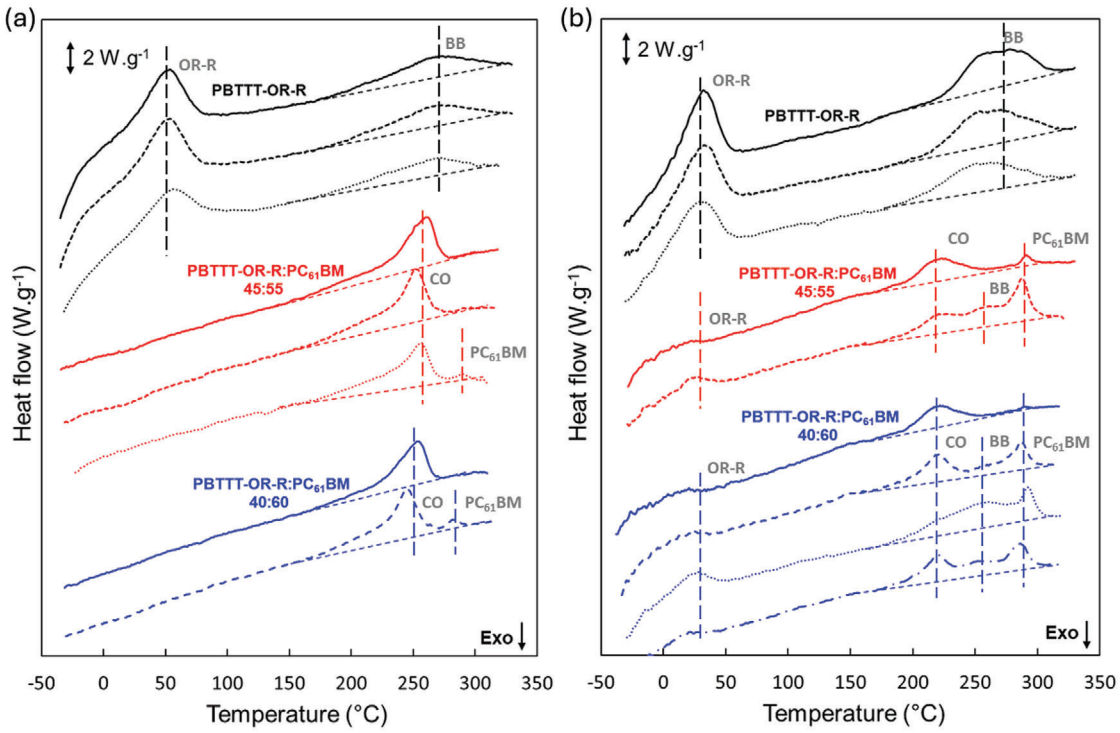

Figure 5. RHC thermograms in heating at 500 K min^{-1} of PBTTT-OR-R, oxidative a) and Stille b), for pristine polymers (black) and 45:55 w/w% (red) and 40:60 w/w% (blue) PBTTT-OR-R:$PC_{61}BM$ mixed compositions, after cooling from 320 °C at 500 K min^{-1} (full), 20 K min^{-1} (dashed), or 5 K min^{-1} (dotted). A thermogram in heating at 500 K min^{-1} of PBTTT-OR-R(S) 40:60 w/w% b), after a quench cooling from 320 to 200 °C, followed by a further cooling from 200 °C at 5 K min^{-1}, is also shown (blue, dash-dotted). Side chain (OR-R), backbone (BB), co-crystal (CO), and $PC_{61}BM$ melting are indicated with vertical lines around their peak maxima.

after slow cooling; ii) transition from the sanidic liquid crystalline state of PBTTT-OR-R to the fully molten state by a broad "backbone melting" trajectory ranging from around 220 to 320 °C. While the endsets of backbone melting of PBTTT-OR-R(O) and PBTTT-OR-R(S) are similar, the ratio of melting enthalpies of side chains against backbones is higher in PBTTT-OR-R(O), suggesting that the absence of homocoupling defects in the oxidative variant allows a more efficient side chain crystallization after ordering of the defect-free backbones when cooled at a similar rate from the melt. The corresponding side chain melting peak temperature is also higher for OR-R(O) than for OR-R(S); iii) co-crystal melting in 45:55 or 40:60 wt.% mixtures with $PC_{61}BM$ in a narrower temperature region with a peak maximum around 250 °C for PBTTT-OR-R(O):$PC_{61}BM$ and around 220 °C for PBTTT-OR-R(S):$PC_{61}BM$. It is clear that *both* PBTTT-OR-R variants show co-crystal formation after mixing with the appropriate amount of $PC_{61}BM$, in contrast with PBTTT-$(OR)_2$, for which *only* the oxidative variant allowed co-crystal formation.[17] However, the ca. 30 K lower melting temperature of the PBTTT-OR-R(S):$PC_{61}BM$ co-crystal compared to the oxidative variant, indicates a thermally less stable co-crystal structure as a result of the homocoupling defects in PBTTT-OR-R(S). This lower thermal stability of the co-crystal against the corresponding Stille polymer is also responsible for the different sensitivity to the preceding cooling rate (vide infra); iv) an eventual melting trajectory of $PC_{61}BM$ crystals with a peak maximum around 290 °C because of *incongruent* melting of the co-crystals[17,37] and crystallization during a preceding slow cooling (vide infra).

The clearly different effect of the preceding cooling rate, ranging from 5 to 500 K min^{-1}, on the RHC thermograms of PBTTT-OR-R(O) and PBTTT-OR-R(S) is also illustrated in Figure 5. The melting trajectories of the pristine polymer as well as the co-crystal of PBTTT-OR-R(O) (Figure 5a) are insensitive to the preceding cooling rates, implying that the ordering of the oxidative variant and its co-crystal with $PC_{61}BM$ is rather robust and not influenced by thermal history. On the contrary, the thermal properties of the co-crystal PBTTT-OR-R(S):$PC_{61}BM$ (Figure 5b) are largely influenced by the preceding cooling rate. After cooling from 320 °C at 500 K min^{-1}, only incongruent melting of the co-crystal is observed. For lower cooling rates, e.g. 20 K min^{-1}, a competition between *co-crystallization* of PBTTT-OR-R(S) with $PC_{61}BM$ *and separate crystallization* of PBTTT-OR-R(S) and $PC_{61}BM$ is derived through the presence of the corresponding melting signals. For even lower cooling rates, e.g. 5 K min^{-1}, the separate PBTTT-OR-R(S) and $PC_{61}BM$ crystallization is dominant at the expense of co-crystallization. We hypothesize that the PBTTT-OR-R(S) polymer (backbones) crystallizes earlier, i.e., at higher temperatures, when cooled relatively slowly, by which the polymer is depleted for co-crystal formation at lower temperatures. When cooled rapidly, this separate polymer backbone crystallization is skipped kinetically, permitting for extensive co-crystal formation at a lower temperature.

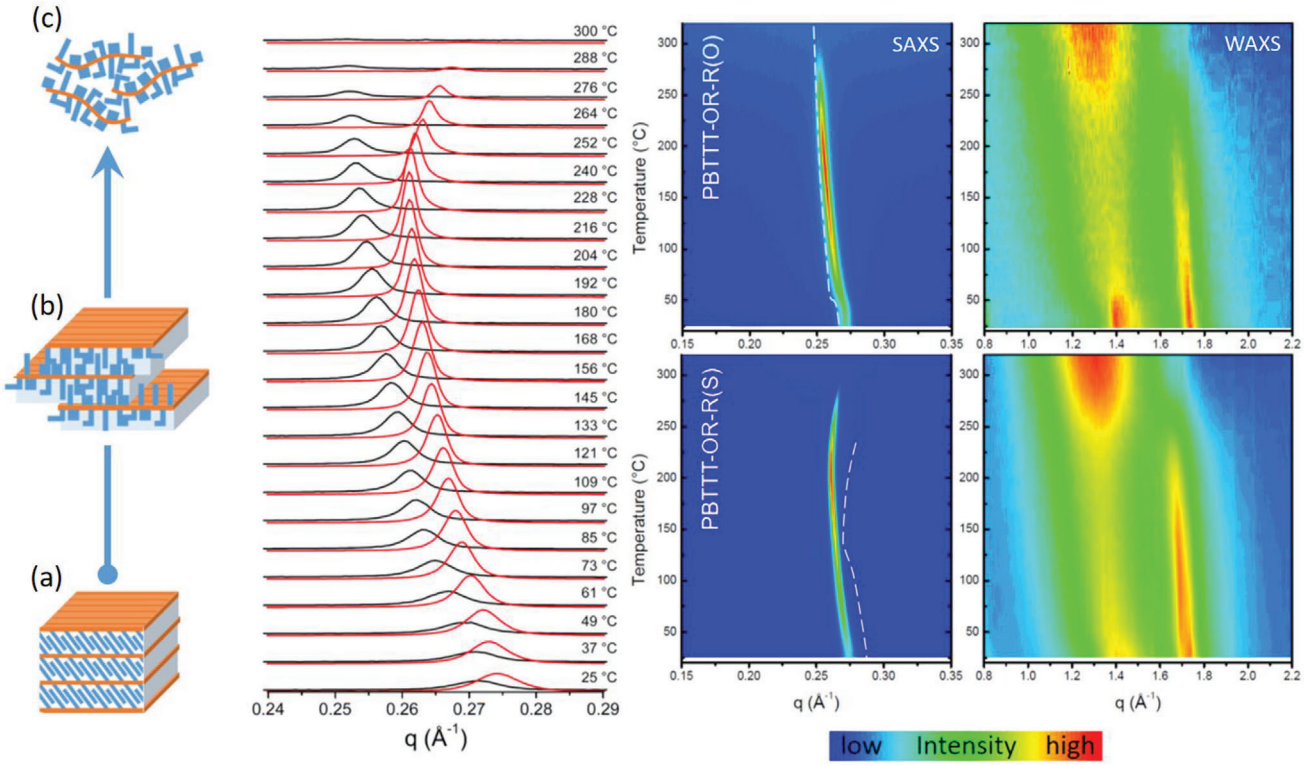

Figure 6. Selected temperature-resolved SAXS patterns of PBTTT-OR-R(O) (black) and PBTTT-OR-R(S) (red) and all top-viewed color-coded SAXS/WAXS data during heating at 50 K min^{-1} after cooling at 20 K min^{-1} for PBTTT(O) and after cooling at 5 K min^{-1} for PBTTT(S) (top panels: SAXS and WAXS of PBTTT-OR-R(O); bottom panels: SAXS and WAXS of PBTTT-OR-R(S). Left: Schematic representation of conversion from the crystalline a) to the sanidic liquid crystalline state b) by side chain (blue lines) melting, followed by backbone (orange lines) melting into the fully molten state c). The dashed white lines in the colored SAXS panels of PBTTT-OR-R(O) and PBTTT-OR-R(S) are from PBTTT-$(OR)_2$(O) and PBTTT(S), respectively (for comparison).[17]

This line of thought implies significantly lower thermal stability of the co-crystals compared to that of the sanidic liquid crystals of the pure Stille polymer. The time spent between 320 °C (the sanidic liquid crystal stability limit, i.e., the endset of the backbone melting signal) and 200 °C (the approximate onset of co-crystal formation during cooling as evidenced by XRD, vide infra) is crucial to permit separate polymer backbone crystallization. Indeed, if this temperature window in the melt of PBTTT-OR-R(S):$PC_{61}BM$ 40:60 wt.% is bridged by a quench cooling (preventing polymer backbone crystallization), co-crystal formation re-appears in competition with polymer backbone crystallization in subsequent cooling from 200 °C, even for a cooling rate of 5 K min^{-1} (see dash-dotted thermogram of Figure 5b). The latter result is further supported by isothermal crystallization experiments (vide infra). All RHC peak assignments rely on direct T-resolved XRD evidence, as explained in more detail below.

2.2.2. T-Resolved XRD of the Pristine Polymers

Figure 6 displays the SAXS and WAXS patterns of the pristine polymers during heating at 50 K min^{-1} after cooling at 20 K min^{-1} for PBTTT(O) and after cooling at 5 K min^{-1} for PBTTT(S). The WAXS reflection at $\approx q = 1.4$ Å^{-1} originates from the crystalline side chain packing, as was clearly demonstrated for pure PBTTT[38] and also detected in PBTTT-$(OR)_2$.[17] It occurs in both PBTTT-OR-R(S) and PBTTT-OR-R(O) and decreases in the temperature range where RHC detects side chain melting. Concomitantly, intensity is added to the broad amorphous halo, also centered at about q = 1.4 Å^{-1}. Across this transition and beyond its endset, the WAXS reflection at $q = 1.74$ Å^{-1} at 25 °C remains but gradually shifts to lower q-values upon heating. This reflection represents the $\pi - \pi$ stacking distance (3.61 Å at 25 °C) of the aromatic rings in stacked polymeric backbones.[17] It only starts weakening in favor of the growing amorphous halo at ≈170 °C, which closely corresponds with the onset of the backbone melting peak in RHC (Figure 5). Traces of this reflection persist up to at least 290 °C, which is close to the backbone melting endset temperature in RHC (Figure 5).

The sequence of structures formed during heating is depicted in the left-side cartoon of Figure 6. The sanidic liquid crystalline state (b), generated from the crystalline state (a), involves freely moving sheets in which the main chain interactions keep the sheets together. The stacking periodicity of the sheets in the crystalline and sanidic states produce SAXS reflections of which the first-order reflection is shown in Figure 6. The SAXS peak position of PBTTT-OR-R(O) remains fairly constant at 0.2712 Å^{-1} (corresponding to a periodicity of 23.2 Å) while being in the crystalline state but drifts to lower q-values while being in the sanidic state, likely as a result of thermal expansion. Similar behavior was observed for PBTTT-$(OR)_2$ prepared using the same

oxidative method.[17] The evolution of the SAXS peak for PBTTT-$(OR)_2$(O) from our earlier work[17] is added to the PBTTT-OR-R(O) SAXS panel using a dashed line in Figure 6. The PBTTT-$(OR)_2$(O) SAXS peak occurs at slightly lower q-values, implying a larger periodicity. The SAXS peak evolution for PBTTT(S), produced via a Stille coupling,[17] is added to the PBTTT-OR-R(S) SAXS panel using a dashed line and clearly occurs at larger q-values, implying a shorter periodicity. The larger periodicity for PBTTT-$(OR)_2$(O) compared to PBTTT(S) relates to the additional oxygen atom in the side chains, which separates the layers somewhat further from each other. The observation that the periodicity for PBTTT-OR-R(S) and PBTTT-OR-R(O) fall in between the R and OR carrying homopolymers suggests that the side by side stacking of dissimilar side chains in common layers leads to an averaged periodicity. However, the actual packing of PBTTT-OR-R(S) and PBTTT-OR-R(O) is different, given that the periodicity of PBTTT-OR-R(S) is smaller than that of PBTTT-OR-R(O) at all temperatures (see Figure 6, the panel with SAXS patterns at selected temperatures). The PBTTT-OR-R(S) layer periodicity at room temperature equals 22.92 Å whereas that of PBTTT-OR-R(O) is 23.2 Å. It is not obvious to extract packing details from the SAXS patterns. This requires simulations in which the chain microstructural differences between the polymers are taken into account, as outlined in the next section.

Note that the SAXS peak position of PBTTT-OR-R(S) after a drift to lower q-values up to ≈170 °C, bends back to higher q-values upon further heating. This cannot be explained in terms of thermal expansion and seems to be a typical feature of Stille cross-coupled polymers since PBTTT(S) shows this behavior too (the dashed line in the PBTTT-OR-R(S) SAXS panel of Figure 6). Note that beyond 170 °C, backbone melting occurs. The evolution to a lower stacking periodicity may follow from a preferred melting of layers with a larger stacking distance, leaving more closely stacked structures up to the highest temperatures. This reasoning implies the existence of different stacking distances across the layer stacks with the experimentally observed SAXS periodicity representing the average. The stability of the individual layers in the sanidic liquid crystals is dominated by their main chain interactions, i.e., the $\pi - \pi$ interactions between the aromatic rings. It is hypothesized that chains with numerous TT coupling mistakes, interact more strongly because of a higher aromatic ring density. Such layers would melt at the highest temperatures. These TT coupled rings do not carry side chains, by which sheets based on TT defective chains can pack more closely. This can explain the associated shorter stack periodicity. The higher stability of layers with TT defective chains also implies a chain selection upon cooling with the TT defective chains gathering into the first forming sanidic layers at the highest temperatures. The absence of TT defects in PBTTT-OR-R(O) explains why for that material no SAXS peak back bending is observed.

2.2.3. Simulation of the Polymer Morphology at 25 and 150 °C

To better understand the crystalline polymer morphology, simulations were performed at 25 °C. The results are displayed in **Figure 7**. As explained in Section 2.1, PBTTT-OR-R(S) contains homocoupling defects in the main chain besides regiochemical irregularities, while PBTTT-OR-R(O) in fact is a copolymer blend

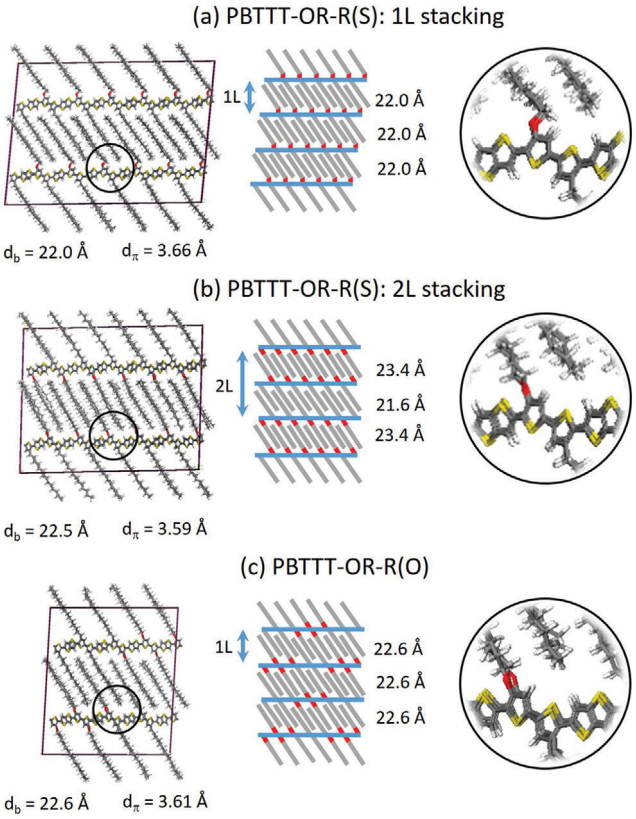

Figure 7. Representation of the simulated organizations of a) defect-free PBTTT-OR-R(S) in 1L and b) 2L arrangement, and of c) PBTTT-OR-R(O). The left side images are last snapshots of 1 ns-long molecular dynamics at 25 °C together with values for the average backbone-to-backbone separation distance, d_b, and the $\pi - \pi$ stacking distance of the main chains, d_p. The middle cartoons represent larger stacks of these snapshots with size indications (main chains in blue and side chains in grey, with red being the oxygen atoms). The right side images are magnifications of the circled regions in the left side snapshots to highlight the oxygen atom connection.

of chains with different amounts of alkyl and alkoxy carrying moieties. Capturing these defects at a statistically relevant level in the simulation is not possible. Therefore, a defect-free PBTTT-OR-R(S) microstructure was assumed. Because of its chain microstructure, the PBTTT-OR-R(S) layer stacking can happen in either a 1L (Figure 7a) or 2L (Figure 7b) fashion, referring at a stacking of layers in which the alkyl and alkoxy side chains are mixed in common layers (1L) or separated in alternating alkyl and alkoxy side chain layers (2L). Strictly, the 2L stacking should produce a reflection at a doubled spacing compared to the 1L stacking mode, which was experimentally not observed, suggesting that the 1L stacking mode is preferred (although the 2L stacking was found to be energetically slightly more stable ($DE = 1.34$ kcal mol^{-1})).

To capture PBTTT-OR-R(O), a representative element was chosen that contains four chain fragments with each having two coupled pairs of alkyl and alkoxy carrying monomers. This leads to mixed alkoxy/alkyl layers with a (1L) periodicity of 22.6 Å. Given the symmetry of the small representative element, the periodic stacking is in fact also of 2L nature as identical features are

reproduced each second layer, as illustrated in the expanded cartoon at the right side of the simulation snapshot in Figure 7c. However, in reality, many different chains are expected to pile up into macroscopic, mixed stacks without internal symmetry. Accordingly, 2L type stacks or XRD reflections cannot be expected. All layers in this representative PBTTT-OR-R(O) case are separated over an identical 22.6 Å, which is larger than the 1L periodicity of PBTTT-OR-R(S), i.e., 22.0 Å, as also observed experimentally. Indeed, the SAXS-based value for PBTTT-OR-R(S) at 25 °C equals 22.9 Å whereas that of PBTTT-OR-R(O) is 23.2 Å. The experimental values are both a bit larger, likely due to the use of too ideal structures in the simulations.

The simulated periodicity at 25 °C, which in earlier work was referred to as the backbone-to-backbone separation distance, d_b, for defect-free PBTTT (21.6 Å) and PBTTT-$(OR)_2$ (22.6 Å) have been reported before.[17] Interestingly, the calculated PBTTT-OR-R(O) d_b value equals that of PBTTT-$(OR)_2$, suggesting that the periodicity in stacks of layers with randomly mixed alkoxy/alkyl side chains is governed by the longest (alkoxy) side chains. This also implies that the alkoxy side chains are coupled to the main chain in a comparable way. This is indeed the case for PBTTT-OR-R(O) in which the oxygen atoms just prolong the linearity of the side chains as a whole, as illustrated in the right-side magnified image. Such a side chain conformation is also seen in defect-free PBTTT-$(OR)_2$.[17] This is not so in 1L stacked PBTTT-OR-R(S), where the ordered and stoichiometric mixing of alkyl and alkoxy side chains induces a kink at the alkoxy oxygen coupling (see magnification at the right side) to maximize interaction between the alkyl and alkoxy chains and by which the periodicity is somewhat reduced. This conformational effect can explain the experimentally observed smaller PBTTT-OR-R(S) stacking periodicity compared to that of PBTTT-OR-R(O). A final remark concerning Figure 7b is added in the Supporting Information (Section 3).

Figure S9 (Supporting Information) reports on the polymer structures at 150 °C. At this temperature, the side chains have lost their crystalline order, as expected for the sanidic liquid crystalline state. Interestingly, all d_b values of the simulations converge to 23 Å, irrespective of the polymer or stack type. The kinks at the alkoxy oxygen coupling in 1L stacked PBTTT-OR-R(S) no longer exist and the main chain conformation is no longer polymer dependent. In reality, d_b of PBTTT-OR-R(S) remains smaller (23.8 Å) than d_b of PBTTT-OR-R(O) (24.3 Å) at 150 °C, as seen in Figure 6 where the PBTTT-OR-R(O) SAXS peak occurs at smaller q-values. This is likely due to main chain defects in PBTTT-OR-R(S) not accounted for in the simulations and which have been suggested to also cause the SAXS peak back bending effect.

2.2.4. T-Resolved XRD of Co-Crystals

Figure S9 (Supporting Information) also includes snapshots of simulated co-crystal structures at 25 °C for PBTTT-OR-R(S) combined with $PC_{61}BM$. Simulations were also performed at 150 °C but hardly differ from those at 25 °C and are hence not explicitly reported nor discussed. These co-crystal structures are very similar to those reported earlier for PBTTT and PBTTT-$(OR)_2$ and are composed of stacked layers from polymers with $PC_{61}BM$ intercalated in between the side chains.[17] This intercalation leads to a simulated increased d_b of 32.3 Å for all polymers. Secondly, the polymer aromatic rings engage in a $\pi-\pi$ stacking, like in the pure polymer, but because of the $PC_{61}BM$ intercalation, d_p is increased from 3.63 to 4.68 Å. These findings are fully consistent with the co-crystal XRD data displayed in **Figure 8**.

The SAXS pattern evolution of PBTTT-OR-R(O) mixed with $PC_{61}BM$ (45:55 w/w%) during heating at 50 K min^{-1} after cooling at 20 K min^{-1} (black curves in the left side panel and the data in the top left color plot of Figure 8) can straightforwardly be interpreted in terms of PBTTT-OR-R(O):$PC_{61}BM$ co-crystals. The peak, which is related to the typical d_b for the co-crystal, remains in place up to when its intensity decreases in the temperature range where RHC identified a melting process, i.e., from roughly 170 till 270 °C. The WAXS reflection of that sample at q = 1.37 $Å^{-1}$ and corresponding to a d_p of 4.59 Å also remains in place up to co-crystal melting, where it fades out and is replaced by a sharper reflection at about the same q-value. This new reflection (together with a set of weaker ones at other q-values) is due to the formation of pure $PC_{61}BM$ crystals in a process called incongruent melting.[17,37] Note that the d_p of 4.59 Å differs from the simulated value (4.68 Å). As the MD simulations cannot capture reality perfectly, small differences between the simulations and the X-ray-probed reality can be expected and should be accepted. Indeed, it is – at this stage – impossible to perform MD simulations on very large representative volumes in which all the defects along the PBTTT-OR-R(S) chains, the polymer chain length distribution, and stacking distortions over the various co-crystal layer stacks are considered. Unlike for PBTTT-OR-R(O):$PC_{61}BM$ co-crystals, the incongruent melting of PBTTT-$(OR)_2$:$PC_{61}BM$ co-crystals also involves the formation of pure PBTTT-$(OR)_2$ crystals.[17,37] The absence of polymer crystal formation in the case of PBTTT-OR-R(O) relates to its lower polymer melting temperature in the mixture compared to the co-crystal melting point.[37]

The scattering data for PBTTT-OR-R(S) mixed with $PC_{61}BM$ during heating after cooling at 5 K min^{-1} can also rather easily be interpreted. The single SAXS peak (represented in blue in the right-side panel of Figure 8 and the data in the bottom left color plot) runs parallel to the SAXS peak evolution of pure PBTTT-OR-R(S) (the track highlighted with a full white line) but slightly shifted to lower q-values. We interpret this shifted polymer SAXS peak as being due to a morphology composed of stacked pure polymer layers, contaminated at various places with intercalated $PC_{61}BM$. Besides $PC_{61}BM$-contaminated polymer layer stacks, the WAXS patterns reveal the existence of pure $PC_{61}BM$ crystals. Indeed, sharp and intense reflections are observed from 25 °C up to ≈295 °C, similar to those generated at high temperatures for PBTTT-OR-R(O) mixed with $PC_{61}BM$. There are no traces of PBTTT-OR-R(S):$PC_{61}BM$ co-crystals for this mixture after cooling at 5 K min^{-1}. The expected SAXS peak evolution for such stacks (i.e., the track of PBTTT-OR-R(O):$PC_{61}BM$ co-crystals) is marked out with a long-dashed white line.

The SAXS pattern evolution of PBTTT-OR-R(S) mixed with $PC_{61}BM$ during heating at 50 K min^{-1} after cooling at 20 K min^{-1} is much more complex. The SAXS pattern at room temperature counts 3 nearby reflections rather than 1 (see the red curves in Figure 8). The middle peak is most intense and shifts to high q-values upon heating. It collides with the high q-value peak at the highest temperatures. The track of this weak peak at high

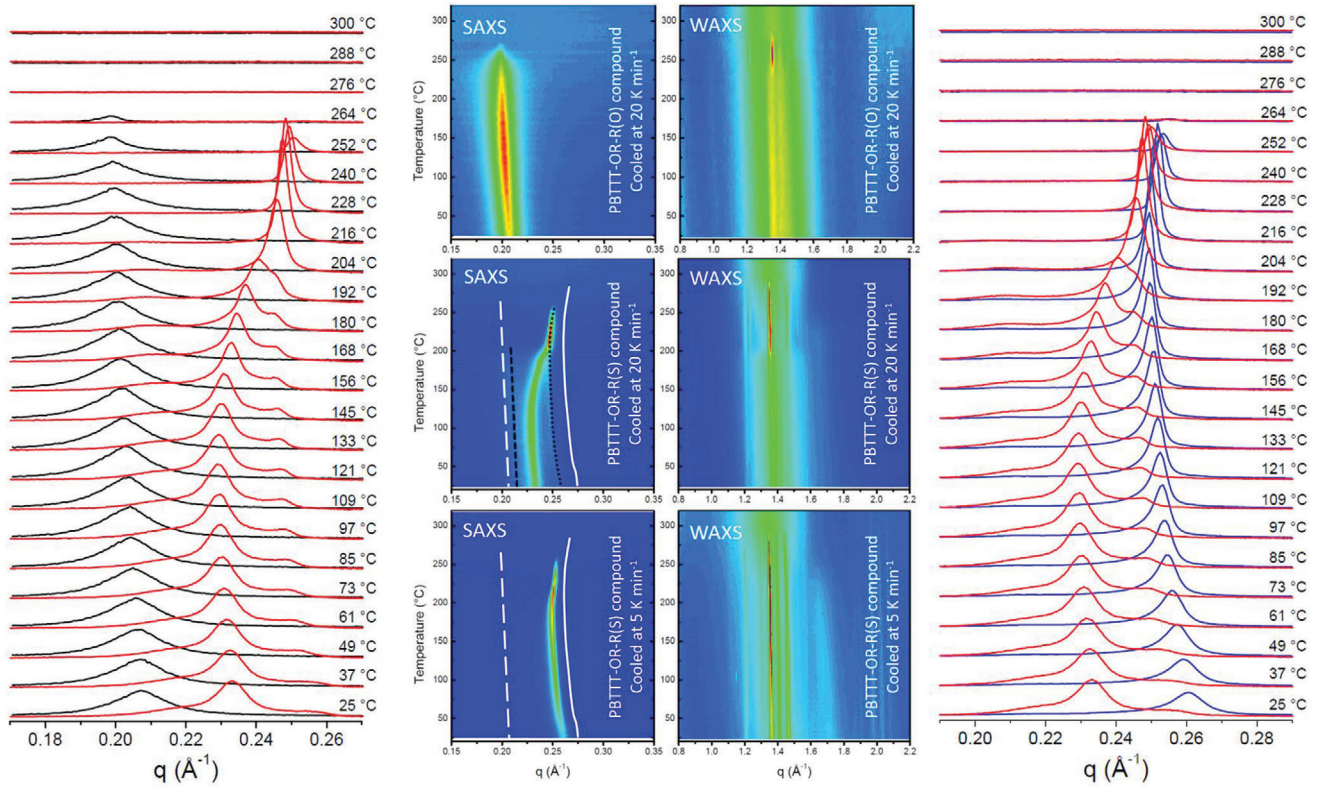

Figure 8. Temperature-resolved XRD in heating at 50 K min^{-1}. Left panel: SAXS of PBTTT-OR-R(O):$PC_{61}BM$ 45:55 w/w% (black) and PBTTT-OR-R(S):$PC_{61}BM$ 40:60 w/w% (red) after cooling at 20 K min^{-1}. Right panel: SAXS of PBTTT-OR-R(S):$PC_{61}BM$ 40:60 w/w% (blue) after cooling at 5 K min^{-1} and PBTTT-OR-R(S):$PC_{61}BM$ 40:60 w/w% (red) after cooling at 20 K min^{-1}. Three middle panels: SAXS (left) and corresponding WAXS (right) data (top viewed and color coded as in Figure 6) after cooling at 20 or at 5 K min^{-1} as indicated in the graphs. The long-dashed white lines are the co-crystal SAXS peak tracks of PBTTT-OR-R(O) of which the patterns are shown in the top panel. The full white lines mark out the SAXS peak track of pure PBTTT-OR-R(S) polymer of which the SAXS data are in Figure 6. The short-dashed and dotted black lines highlight the SAXS peak evolutions of respectively polymer-contaminated co-crystals and $PC_{61}BM$-contaminated PBTTT-OR-R(S) polymer in PBTTT-OR-R(S):$PC_{61}BM$ 40:60 w/w% when cooled at 20 K min^{-1}. Note that the intensity of some WAXS reflections exceeded the adopted color scale. These reflections (which are due to $PC_{61}BM$ crystals) are colored in purple.

q-values is highlighted with a dotted black line and closely follows the track of the SAXS peak for this sample during heating after cooling at 5 K min^{-1}. Therefore, it can also be assigned to $PC_{61}BM$ contaminated polymer layer stacks. The weak SAXS peak at low *q*-values (highlighted using a short-dashed black line) can be associated with polymer contaminated PBTTT-OR-R(S):$PC_{61}BM$ co-crystals, to be imagined as co-crystal layers in which some of the spaces between the side branches are left vacant without $PC_{61}BM$ and by which the polymer backbones on average approach somewhat closer than in pure co-crystals. The expected SAXS peak track of the latter is marked out with a long-dashed white line. Finally, it is proposed that the middle SAXS peak is associated with mixed layer stacks in which contaminated polymer and contaminated co-crystal layers are randomly mixed, and of which the peak position is related to the relative amount of the constituting layers. The shift of this peak to the peak associated with contaminated polymer layers upon heating reflects a progressively reduced presence of (contaminated) co-crystal layers in these mixed stacks. In other words, $PC_{61}BM$ is progressively expelled from these stacks upon heating, as illustrated schematically in **Figure 9**. Once this peak coincides with the (contaminated) polymer peak position, no co-crystal layers are left. This happens at about 200 °C while concomitantly, reflections due to $PC_{61}BM$ crystals strengthen in WAXS. Indeed, weak $PC_{61}BM$ reflections are in fact already present in the room temperature WAXS patterns (but hardly visible) and just intensify above 200 °C. Note that for PBTTT-OR-R(O):$PC_{61}BM$ and PBTTT-$(OR)_2$(O):$PC_{61}BM$ co-crystals, the formation of $PC_{61}BM$ crystals is also observed after the final co-crystal melting, but that in this case the co-crystal remains stable *without* a compositional change till melting, so *without* gradual exclusion of $PC_{61}BM$.[17,37]

The T-resolved XRD results in cooling at 20 K min^{-1} after the heating runs shown in Figure 8 for PBTTT-OR-R(O):$PC_{61}BM$ 45:55 w/w% are given in Figure S10 (Supporting Information) and for PBTTT-OR-R(S):$PC_{61}BM$ 40:60 w/w% in Figure S11 (Supporting Information). The SAXS and WAXS data of Figure S10 (Supporting Information) are consistent with pure co-crystallization from 200 °C onward, with no indications of separate $PC_{61}BM$ or polymer crystal formation. The XRD cooling data of PBTTT-OR-R(S):$PC_{61}BM$ in Figure S11 (Supporting Information) reveal the formation of separate (contaminated) polymer layers (in SAXS) and pure $PC_{61}BM$ crystals at ≈225 °C. The latter remains down to the lowest temperatures (WAXS evidence)

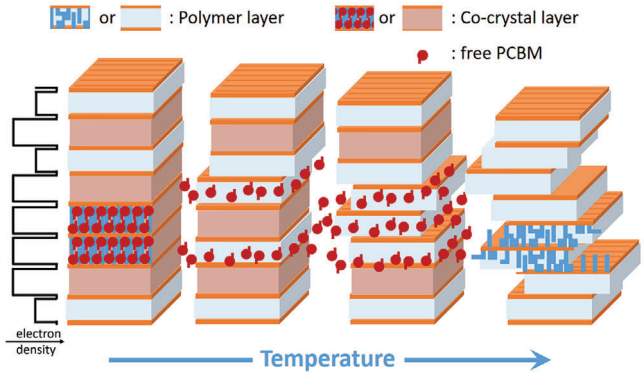

Figure 9. Visualization of the progressive $PC_{61}BM$ exclusion out of the mixed layer stacks in PBTTT-OR-R(S):$PC_{61}BM$ blends during heating at 50 K min^{-1} after cooling at 20 K min^{-1}. The mixed stacks are composed out of randomly positioned polymer and co-crystal layers. The average stack periodicity and total stack height in this cartoon is decreasing with increasing temperature because the polymer layers are thinner than the co-crystal layers. The electron density profile on the left side shows that the density of the co-crystal layers is lower than that of the polymer layers because of the open $PC_{61}BM$ spheres. Note that the contaminations in the polymer and co-crystal layers are not shown in this cartoon. Contamination in the polymer layers refers to a random distribution of accidentally included $PC_{61}BM$, whereas in co-crystal layers it refers to randomly positioned $PC_{61}BM$ absences.

but the former transform into mixed layer stacks in which the share of co-crystal layers increases with decreasing temperature. The events observed during heating are thus reproduced during cooling in reversed order. The earliest formed (contaminated) polymer layers are progressively infused with not yet crystallized $PC_{61}BM$. Already crystallized $PC_{61}BM$ remains in its pure crystalline state. Recall that reflections due to pure $PC_{61}BM$ crystals are also present at the lowest temperatures in the XRD data of PBTTT-OR-R(S):$PC_{61}BM$ during heating but that these reflections are hardly visible because the color scale was adopted to reveal the massive $PC_{61}BM$ crystallization upon heating beyond 200 °C (Figure 8).

In case of a slower cooling at 5 K min^{-1}, *no* mixed stacks of randomly positioned (contaminated) polymer and (contaminated) co-crystal layers are formed. Only separate (contaminated) PBTTT-OR-R(S) polymer stacks and $PC_{61}BM$ crystals are formed (Figure 8). These findings are the basis of the hypothesis formulated earlier at the RHC data discussion (Figure 5).

2.2.5. SAXS Modeling of Mixed Polymer and Co-Crystal Layer Stacks

Interpreting the middle of the three PBTTT-OR-R(S):$PC_{61}BM$ 40:60 w/w% SAXS reflections after cooling at 20 K min^{-1} (Figure 8) in terms of mixed stacks composed of randomly positioned (contaminated) polymer and (contaminated) co-crystal layers is not obvious and calls for further verification. Therefore, selected SAXS patterns of this mixture were modeled in terms of the presumed mixed layer structure and compared with the experimental patterns.

Figure 10 displays the experimental SAXS patterns (green curves) at 73 °C (top panel) and 180 °C (bottom panel). Both temperatures are above the side chain melting temperature range

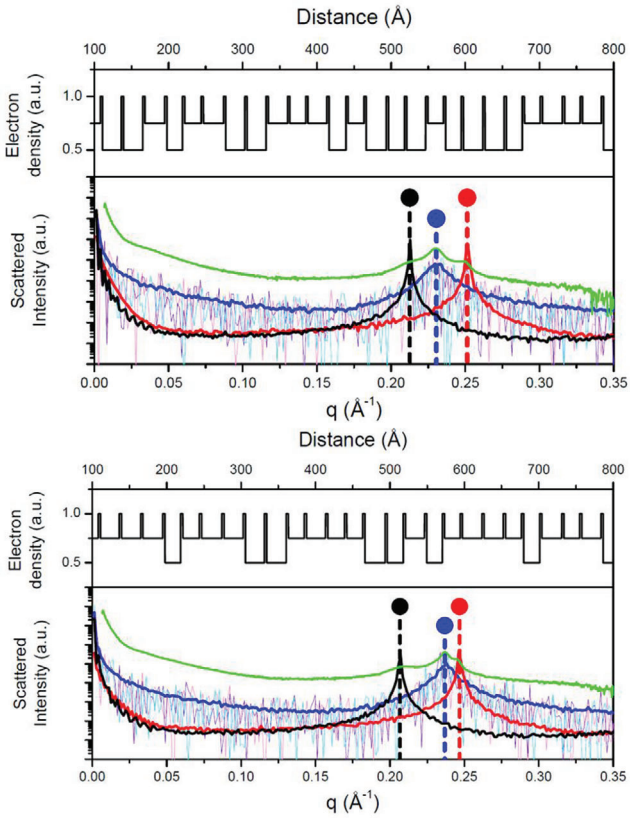

Figure 10. SAXS pattern modeling of PBTTT-OR-R(S):$PC_{61}BM$ 40:60 w/w% in heating at 50 K min^{-1} after cooling at 20 K min^{-1}. The top panel 73 °C and the bottom panel 180 °C, with the experimental patterns in green, the modeled mixed stack patterns in blue, the modeled (contaminated) polymer stack patterns in red, and the modeled (contaminated) co-crystal patterns in black. Peak positions are highlighted using dots on dashed lines in the corresponding colors. The thin magenta, cyan, and purple graphs are modeled SAXS patterns of single mixed layer stacks, whereas the thick blue curves represent average SAXS patterns of 100 different mixed stacks. Fragments of the electron density profiles that are at the basis of the mixed stack patterns are included on top of the graphs. The (relative) electron density of the backbone layers was set at 1, that of the polymer side chain layers at 0.75, and that of $PC_{61}BM$ intercalated side chain layers at 0.5.

and are selected because in both cases the three peaks are present, yet very much shifted. From the q-values of the three SAXS peaks, three stack periods (P_C, P_P, and P_M) were derived and assumed to be due to (contaminated) co-crystal stacks (black marker in Figure 10, P_C), (contaminated) polymer stacks (red marker, P_P), and mixed (contaminated) polymer/co-crystal stacks (blue marker, P_M). The fraction of polymer layers in the mixed stacks, φ, was calculated by solving the following equation for:

$$P_M = \varphi P_P + (1 - \varphi)\, P_C \quad (1)$$

This yielded φ values of 0.5 and 0.78 at 73 and 180 °C, respectively.

Next, 1D electron density profiles, $\rho(x)$, of stacks of 5200 periods were numerically produced, of which the probability of adding a polymer layer was given by φ and of adding a co-crystal

layer by $(1-\varphi)$. Each layer was flanked by backbone sheets of high electron density, given the sulfur atoms in the repeating units. The layer thickness (given by P_P or P_C) equals the distance between the flanking backbone sheets. The nature of the layers (polymer or co-crystal) is given by the characteristic periodicity and electron density. The thickness of the backbone sheet was fixed at 3 Å and the electron density arbitrarily at 1.0. The electron density of the polymer layers was set at 0.75 and that of co-crystal layers at 0.5. The lower density of the co-crystal layers stems from the open nature of the $PC_{61}BM$ spheres. The electron density values are meant to be relative, not absolute, and were chosen to ultimately lead to scattering patterns that resemble the experimental ones. The influence of the relative electron density values is discussed in Figure S12 (Supporting Information).

During numerical stack building, the actual layer thicknesses were permitted to randomly vary over an interval of ±0.5 Å around P_P or P_C. In that way some paracrystalline disorder was introduced. Fragments of the ultimate layer stacks are displayed in the top panels of the images in Figure 10.

The scattered waves, $F(q)$, of the stacks were obtained via the following Fourier transformation:

$$F\ (q) = 2\int_0^{x_{end}} \rho\,(x)\cos\,(qx)\,dx \tag{2}$$

with x_{end} the full stack size and q the modulus of the scattering vector, which for experimental patterns relates to the scattering angle 2θ, as $q = 4\pi sin\theta/\lambda$, with λ the X-ray wavelength. In a next step, theoretical powder patterns, $I(q)$, were generated via:

$$I\ (q) = F(q)^2/4\pi q^2 \tag{3}$$

The use of a *cos* transformation (Equation 2) assumes symmetric stacks with a mirror plane at $x = 0$. In fact, 5200 layers are assumed on both sides of the stack center at $x = 0$. Examples of such $I(q)$ results are given by the thin magenta, purple, and cyan curves in Figure 10. Each curve relates to a stack with identical φ but different random placements of the polymer and co-crystal layers. They appear extremely noisy but in fact this is not "noise". It reflects the specific layer placements. Real systems contain many different stacks. Therefore, the scattering of 100 different stacks (with the same φ) was calculated and averaged. The results are the dark blue curves in Figure 10, which reveal a peak at the q value related to P_M (blue dashed line with dot). In addition, pure polymer (red curves) and pure co-crystal (black curves) were calculated using an identical approach with either only polymer or co-crystal layers.

The following observations can be made based on these model calculations: A) mixed stacks indeed produce SAXS peaks at the composition averaged period; B) mixed stack SAXS peaks are rather broad because of stacking irregularities and therefore their peak width has little relation with the actual stack height; C) mixed stacks produce a higher overall background compared to polymer or co-crystal stacks due to density fluctuations from the stack irregularities. Such scatter is particularly noticeable at very low q-values as a result of "random fluctuations" in composition at larger length scales.

Given observation (A), it is possible to calculate φ with equation (1) from the position of the mixed stack SAXS peak and its related periodicity P_M. The temperature dependent q-values of the middle SAXS peak for PBTTT-OR-R(S):$PC_{61}BM$ 40:60 w/w% during heating at 50 K min^{-1} (values based on the data in Figure 8) and subsequent cooling at 20 K min^{-1} (from the middle peaks in Figure S11, Supporting Information) can be found in the top panel of **Figure 11**. Equation (1) furthermore requires values for P_C and P_P, which were obtained by linear and quadratic approximations and extrapolations of the SAXS peaks at lower (for P_C) and higher (for P_P) q-values from the mixed stack peak.

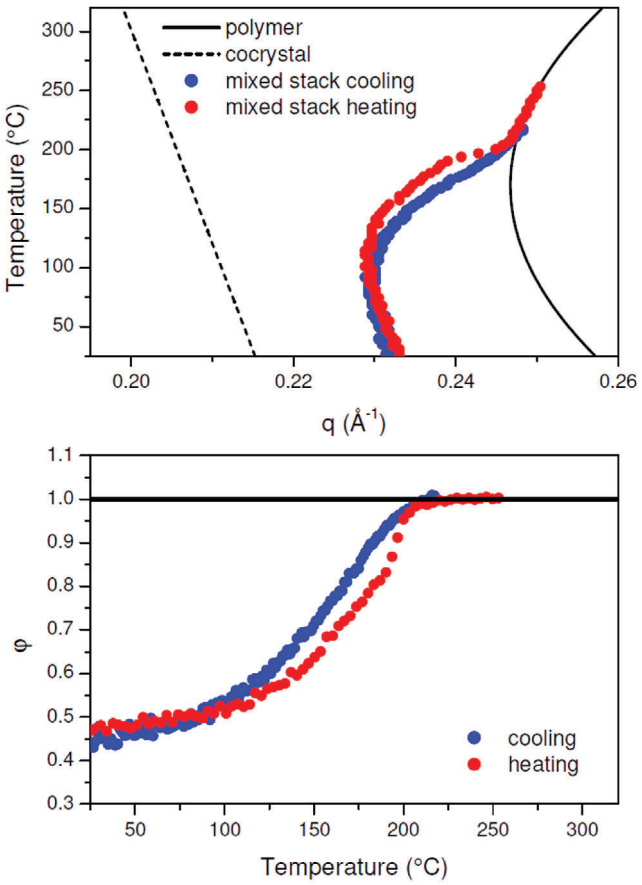

Figure 11. Top: Summary of pertinent SAXS peak positions for PBTTT-OR-R(S):$PC_{61}BM$ 40:60 w/w% during heating at 50 K min^{-1} and cooling at 20 K min^{-1}. The pure (contaminated) polymer (full black) and co-crystal (dashed black) stack peaks are based on a linear (co-crystal) and second-order polynomial fit (polymer) approximation of the real data during heating. Bottom: φ value as a function of temperature for PBTTT-OR-R(S):$PC_{61}BM$ 40:60 w/w% after cooling at 20 K min^{-1} and during heating at 50 K min^{-1}.

The bottom panel in Figure 11 displays the resulting φ values as a function of temperature for heating at 50 K min^{-1} and cooling at 20 K min^{-1}. φ is increasing with temperature as a result of the progressive $PC_{61}BM$ exclusion. This analysis was not meaningful for cooling at 5 K min^{-1} because at this rate no mixed stacks are formed. Here only separate (contaminated) polymer stacks in combination with $PC_{61}BM$ crystals were observed.

While the homocoupling-free PBTTT-OR-R(O) polymer leads to robust co-crystals (see Figures 5 and 8), the homocoupling

defects in PBTTT-OR-R(S) clearly lead to thermally less stable co-crystals with a high sensitivity to the applied process conditions. The residence time above 200 °C is crucial for the balance between co-crystal formation and separate crystallization of PBTTT-OR-R(S) and $PC_{61}BM$. The faster the temperature window above 200 °C is bridged (starting from the melt at high temperature, e.g. 320 °C), the more co-crystallization occurs. This happens after cooling at 500 K min^{-1} in RHC. In the subsequent heating, only incongruent melting of the PBTTT-OR-R(S):$PC_{61}BM$ co-crystal is observed (see Figure 5). The lower the cooling rate in this temperature window, the more co-crystal formation is suppressed, as noticed by cooling at 20 K min^{-1} and even more at 5 K min^{-1}. The faster crystallization kinetics (with smaller supercooling) of the polymer against the co-crystal, together with the lower thermal stability of the co-crystal, are the cause of these observations.

This effect is further illustrated in Figure S13 (Supporting Information) by the RHC results after different isothermal crystallizations of PBTTT-OR-R(S):$PC_{61}BM$ 40:60 w/w% at temperatures above and below 200 °C. At 200 °C and higher temperatures, only PBTTT-OR-R(S) and $PC_{61}BM$ are formed, as in a eutectic binary system. Below 200 °C, PBTTT-OR-R(S), $PC_{61}BM$, *and* co-crystal formation are in competition. These results are in agreement with the crystallization in cooling at 5 K min^{-1} from 200 °C after a quench cooling from 320 to 200 °C (compare the thermogram after isothermal crystallization at 195 °C of Figure S13 (Supporting Information) with the blue dash-dotted thermogram of Figure 5b).

The striking difference between the robust co-crystals of homocoupling-free PBTTT-OR-R(O) and the thermally less stable co-crystals of PBTTT-OR-R(S) containing homocoupling defects, is important for designing optoelectronic devices with optimized performance, as discussed below.

2.3. Impact of Polymer Defects on Device Stability Upon Thermal Annealing

In previous work, we have shown for PBTTT-$(OR)_2$ that a large number of homocoupling defects hinder co-crystal formation.[17] As the strength of the intermolecular (polymer:fullerene) CT absorption directly correlates to the number of donor–acceptor contacts,[39] this results in a lower photodiode device EQE in the spectral region of CT absorption.[17] To quantify the reduced donor–acceptor interfacial area upon thermal annealing, BHJ organic photodiodes were fabricated, using the processing conditions optimized before (see Supporting Information)[17,30] and applying the same ratios as used for all previous analyses (i.e., 40:60 w/w% for the Stille and 45:55 w/w% for the oxidative polymer), and the EQE was determined via Fourier-transform photocurrent spectroscopy, revealing the CT absorption band.[40] Spectra normalized at 2.3 eV, at the polymer absorption peak, are shown in **Figure 12a**. Upon annealing at 150 or 200 °C for 10 min, a progressive drop in CT absorption is observed for the PBTTT-OR-R(S):$PC_{61}BM$ mixture. Such a decrease is present to a much lesser extent for the homocoupling-free PBTTT-OR-R(O):$PC_{61}BM$ film. We quantify this decrease by comparing the reduction in CT absorption at 850 nm with respect to the non-annealed blends. In the case of PBTTT-OR-R(S):$PC_{61}BM$, CT absorption diminishes by ≈40% when annealing at 150 °C and 60% when annealing at 200 °C. In contrast, for the PBTTT-OR-R(O):$PC_{61}BM$ devices, this decline is only of 10 and 25%, respectively. Furthermore, the absorptive feature around 1.75 eV, which is attributed to a pure $PC_{61}BM$ phase,[39] clearly gets more pronounced after annealing, implying fullerene crystal formation (Figure 12a; Figure S14a, Supporting Information). Also in the more application-relevant 20:80 w/w% polymer:$PC_{61}BM$ devices, this trend holds true and we observed deteriorated CT absorption and an increase in the $PC_{61}BM$ pure phase (Figure S14b, Supporting Information). $PC_{61}BM$ phase separation is also evident from the optical microscopy images of the blends. While no clear sign of phase separation was found before annealing in the 40:60 w/w% PBTTT-OR-R(S) devices (Figure 12c), macroscopic size (1–10 µm) $PC_{61}BM$ crystal formation can indeed be observed after annealing at 150 °C (Figure 12d). Upon annealing at 200 °C, the $PC_{61}BM$ crystal sizes further increased (to 10–40 µm) (Figure 12e; Figure S15, Supporting Information), being consistent with additional migration of intercalated $PC_{61}BM$ to pure fullerene domains. On the other hand, the homocoupling-free PBTTT-OR-R(O):$PC_{61}BM$ mixture, already showing a stronger CT absorption from the start, did not show a clear $PC_{61}BM$ absorption feature after annealing at 150 or 200 °C (Figure 12a; Figure S14, Supporting Information), in line with the absence of macroscopic-sized crystals, neither before or after annealing (Figure S16, Supporting Information), illustrating the stability of the intercalated morphology. As a consequence, and importantly, active layer annealing at temperatures of 150 °C and above, as commonly done for PBTTT:$PC_{61}BM$ type blends to enhance crystallinity,[27] seems to instigate phase separation and a lower degree of intermixing if the presence of homocoupling defects in the polymer structure is not carefully remediated.

More generally, photocurrent deteriorates by almost an order of magnitude at −1 V after annealing the PBTTT-OR-R(S):$PC_{61}BM$ devices at 150 and 200 °C, for both 40:60 and 20:80 w:w% devices (Figure 12b; Figure S17a,c, Supporting Information), while in the case of PBTTT-OR-R(O) there is only 20% decrease at −1 V after annealing at 150 and 200 °C for the 45:55 w/w% devices (Figure 12b; Figure S17b, Supporting Information) and even a slight improvement of the photocurrent when annealing the 20:80 w/w% devices at 150 °C (Figure S17d, Supporting Information). Furthermore, the photocurrent of the as-prepared 45:55 w/w% PBTTT-OR-R(O):$PC_{61}BM$ device under solar illumination is lower than that of the 40:60 w/w% PBTTT-OR-R(S):$PC_{61}BM$ device, indicating strongly reduced electron transport pathways in the former through the absence of a significant $PC_{61}BM$ phase and molecular intermixing at the 45:55 w/w% blend stoichiometry used. These pathways are more present in PBTTT-OR-R(S):$PC_{61}BM$, but upon annealing, $PC_{61}BM$ is extracted out of the mixed phase, reducing exciton dissociation and hereby the photocurrent. For optimal OPD performance, a low current under dark conditions is also desired. In the 20:80 w/w% devices, this dark current remained more stable after annealing in the PBTTT-OR-R(O) compared to the PBTTT-OR-R(S) devices (Figure S17c,d, Supporting Information). Finally, the response speed of the detectors is not affected by the presence of homocoupling defects (Figure S18, Supporting\ Information).

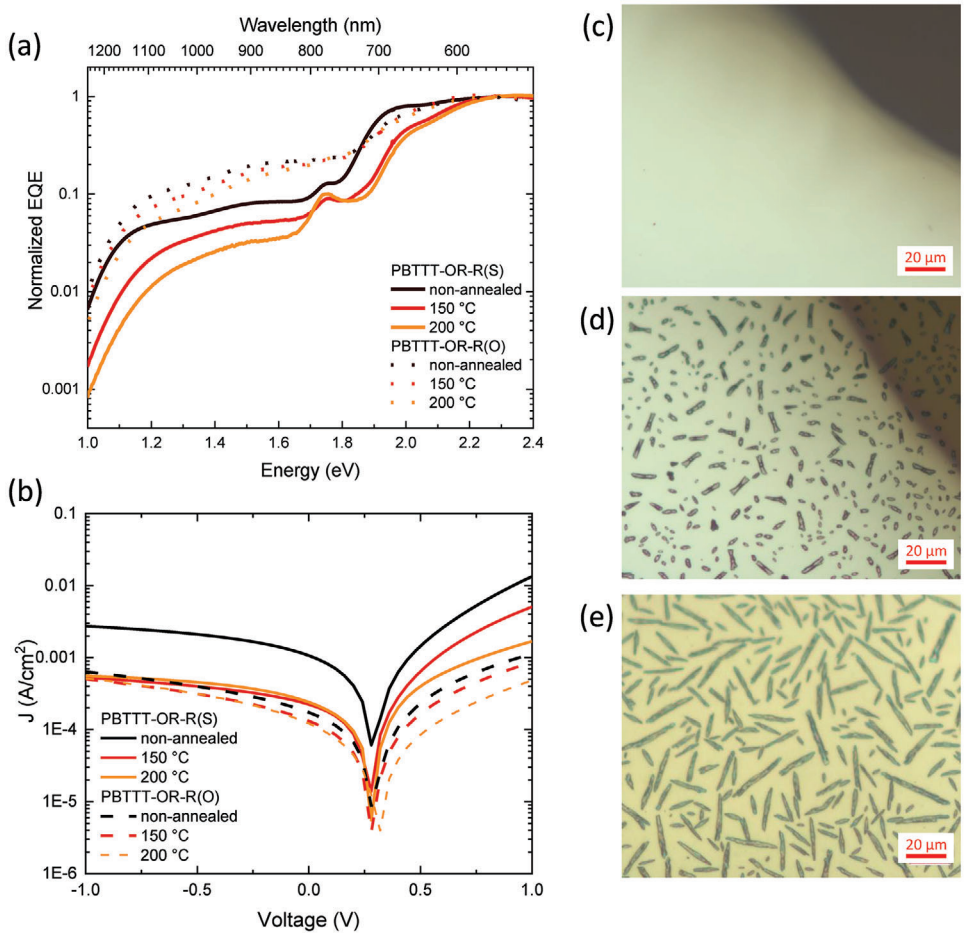

Figure 12. a) In-band normalized EQE for the photodiodes based on mixtures of PBTTT-OR-R(S) or PBTTT-OR-R(O) with $PC_{61}BM$ at 40:60 and 45:55 w/w%, respectively, before and after annealing at 150 and 200 °C. The CT absorption is significantly lower when using the Stille polymer, especially after annealing. A distinct absorption feature attributed to $PC_{61}BM$ can also be seen at ≈1.75 eV.[39] b) Light current density versus voltage plots for the PBTTT-OR-R(S):$PC_{61}BM$ (40:60 w/w%) and PBTTT-OR-R(O) (45:55 w/w%) devices, demonstrating a significantly reduced light current for PBTTT-OR-R(S) after annealing at 150 °C. c) Optical microscopy images at 50x magnification for the non-annealed, and (d) & (e) for the annealed PBTTT-OR-R(S):$PC_{61}BM$ devices at 150 and 200 °C, respectively, showing the appearance of macroscopic crystals of $PC_{61}BM$.

While these insights are certainly highly relevant for applications relying on the maximization of the interfacial area, such as CT absorption-based NIR OPD devices, this work also more generally shows that structural defects may have a profound impact on the morphology and stability of conjugated polymer blends, most likely also beyond the PBTTT derivatives studied here.

3. Conclusion

Further exploring the alkoxy–alkyl derivative of the prototype semi-crystalline conjugated polymer PBTTT is relevant from an application point of view because it represents the best compromise for organic narrow-band near-infrared photodetection, combining PBTTT-like intercalation behavior with PBTTT-$(OR)_2$-like enhanced charge-transfer absorption at longer wavelengths.[30] Additionally, fundamental analysis becomes much more clear and new valuable insights can be achieved by comparing these alternating conjugated polymer systems in the presence and absence of homocoupling defects. The oxidative, homocoupling-free, variant PBTTT-OR-R(O) as well as the Stille variant PBTTT-OR-R(S) (with 19% homocoupling defects) can both form co-crystals when stoichiometrically mixed with $PC_{61}BM$. However, the PBTTT-OR-R(S):$PC_{61}BM$ co-crystal shows much lower thermal stability because of the presence of these defects. Whereas the PBTTT-OR-R(O):$PC_{61}BM$ co-crystal is stable up to at least 260 °C and not influenced by the applied cooling rate during co-crystallization, the properties of the co-crystal of the Stille variant are highly dependent on the thermal processing conditions. Fast cooling from the melt, e.g. at 500 K min^{-1}, favors *co-crystallization* of PBTTT-OR-R(S) and $PC_{61}BM$, whereas at slow cooling conditions, e.g. at 5 K min^{-1}, a *separate crystallization* of PBTTT-OR-R(S) and $PC_{61}BM$ is dominant. For intermediate cooling rates, e.g. 20 K min^{-1}, a competition between both crystallization mechanisms is seen. The latter conditions can be described by SAXS pattern modeling in terms of three different layer stacks, revealing also that $PC_{61}BM$ is progressively expelled from the mixed layer stacks upon heating at 20 K min^{-1}. Importantly, these findings also translate to the device level. EQE

spectra for PBTTT-OR-R:$PC_{61}BM$ bulk heterojunction photodiodes after thermal annealing, e.g. at 150 and 200 °C, confirm that device performance is severely deteriorated in case of PBTTT-OR-R(S), while the thermally robust co-crystals of homocoupling-free PBTTT-OR-R(O) allow a more reproducible and reliable device outcome. This work stipulates the importance of detailed elucidation of the accurate chemical structure of conjugated polymers in order to draw rigorous conclusions on materials-device properties relationships and to achieve optimal device performance.

Supporting Information

Supporting Information is available from the Wiley Online Library or from the author.

Acknowledgements

The authors thank the Research Foundation – Flanders (FWO Vlaanderen) for continuing financial support (projects G0D0118N, G0B2718N, 1S50820N, 11D2618N, DUBBLE – I001919N, and the Scientific Research Community "Supramolecular Chemistry and Materials" – W000620N), as well as the European Research Council (ERC, grant agreement 864625). Furthermore, the authors acknowledge funding from the European Commission Horizon 2020 Future and Emerging Technologies (FET) project MITICS (964677). The computational resources in Mons are supported by the FNRS "Consortium des Equipements de Calcul Intensif-CECI" program Grant No. 2.5020.11. D.B. is a FNRS Research Director.

Conflict of Interest

The authors declare no conflict of interest.

Author Contributions

Z.L., J.V., and P.M. contributed equally to this work. Z.L. performed the RHC and T-resolved XRD measurements and interpreted the data. J.V. synthesized and characterized the materials, performed MALDI-ToF, UV–vis, optical microscopy, and photodiode measurements, and did the data analysis. P.M. performed the STM experiments and analyzed the resulting data. St.M. contributed to the acquisition and analysis of the STM data. M.H. contributed to the T-resolved XRD measurements. Si.M. contributed to the sensitive EQE measurements and data analysis. V.L. performed the simulations. D.B. supervised the simulation work and contributed to the discussions. N.V.B. supervised the RHC part of the project. L.L. co-supervised the materials synthesis work. G.C. supervised the STM experiments and contributed to the discussions. K.V. supervised the photodiode measurements and part of the overall project. B.G. performed and supervised the T-resolved XRD measurements, data analysis, and interpretation in relation to the RHC and simulation data. B.V.M. contributed to the interpretation of the RHC and T-resolved XRD measurements and co-supervised the project. W.M. supervised the materials synthesis and characterization work and was in charge of the overall project. Z.L, J.V., B.G, W.M., and B.V.M. conceived the idea and wrote the manuscript and all authors contributed to the revision and editing.

Data Availability Statement

The data that support the findings of this study are available from the corresponding author upon reasonable request.

Keywords

co-crystal thermal stability, defect-free synthesis, fullerene intercalation, homocoupling, organic photodetectors

Received: July 29, 2024
Revised: September 5, 2024
Published online: October 3, 2024

[1] L. Ding, Z. Yu, X.-Y. Wang, Z.-F. Yao, Y. Lu, C.-Y. Yang, J.-Y. Wang, J. Pei, *Chem. Rev.* **2023**, *123*, 7421.
[2] A. Wadsworth, Z. Hamid, J. Kosco, N. Gasparini, I. McCulloch, *Adv. Mater.* **2020**, *32*, 2001763.
[3] G. Zhang, F. R. Lin, F. Qi, T. Heumüller, A. Distler, H.-J. Egelhaaf, N. Li, P. C. Chow, C. J. Brabec, A. K. Jen, H.-L. Yip, *Chem. Rev.* **2022**, *122*, 14180.
[4] J. Vanderspikken, W. Maes, K. Vandewal, *Adv. Funct. Mater.* **2021**, *31*, 2104060.
[5] H. Bronstein, C. B. Nielsen, B. C. Schroeder, I. McCulloch, *Nat. Rev. Chem.* **2020**, *4*, 66.
[6] R. M. Pankow, B. C. Thompson, *Polymer* **2020**, *207*, 122874.
[7] S. Holliday, Y. Li, C. K. Luscombe, *Prog. Polym. Sci.* **2017**, *70*, 34.
[8] Y. Cui, Y. Xu, H. Yao, P. Bi, L. Hong, J. Zhang, Y. Zu, T. Zhang, J. Qin, J. Ren, Z. Chen, C. He, X. Hao, Z. Wei, J. Hou, *Adv. Mater.* **2021**, *33*, 2102420.
[9] G. Pirotte, P. Verstappen, D. Vanderzande, W. Maes, *Adv. Electron. Mater.* **2018**, *4*, 1700481.
[10] C. Cordovilla, C. Bartolomé, J. M. Martínez-Ilarduya, P. Espinet, *ACS Catal.* **2015**, *5*, 3040.
[11] N. S. Gobalasingham, B. C. Thompson, *Prog. Polym. Sci.* **2018**, *83*, 135.
[12] K. H. Hendriks, W. Li, G. H. Heintges, G. W. Van Pruissen, M. M. Wienk, R. A. Janssen, *J. Am. Chem. Soc.* **2014**, *136*, 11128.
[13] F. Lombeck, H. Komber, D. Fazzi, D. Nava, J. Kuhlmann, D. Stegerer, K. Strassel, J. Brandt, A. D. de Zerio Mendaza, C. Müller, W. Thiel, M. Caironi, R. Friend, M. Sommer, *Adv. Energy Mater.* **2016**, *6*, 1601232.
[14] T. Vangerven, P. Verstappen, J. Drijkoningen, W. Dierckx, S. Himmelberger, A. Salleo, D. Vanderzande, W. Maes, J. V. Manca, *Chem. Mater.* **2015**, *27*, 3726.
[15] G. H. Heintges, R. A. Janssen, *RSC Adv.* **2019**, *9*, 15703.
[16] I. McCulloch, M. Heeney, C. Bailey, K. Genevicius, I. MacDonald, M. Shkunov, D. Sparrowe, S. Tierney, R. Wagner, W. Zhang, M. L. Chabinyc, R. J. Kline, M. D. McGehee, M. F. Toney, *Nat. Mater.* **2006**, *5*, 328.
[17] J. Vanderspikken, Z. Liu, X. Wu, O. Beckers, S. Moro, T. J. Quill, Q. Liu, A. Goossens, A. Marks, K. Weaver, M. Hamid, B. Goderis, E. Nies, V. Lemaur, D. Beljonne, A. Salleo, L. Lutsen, K. Vandewal, B. Van Mele, G. Costantini, N. Van den Brande, W. Maes, *Adv. Funct. Mater.* **2023**, *33*, 2309403.
[18] M. J. Lee, D. Gupta, N. Zhao, M. Heeney, I. McCulloch, H. Sirringhaus, *Adv. Funct. Mater.* **2011**, *5*, 932.
[19] J. E. Cochran, M. J. Junk, A. M. Glaudell, P. L. Miller, J. S. Cowart, M. F. Toney, C. J. Hawker, B. F. Chmelka, M. L. Chabinyc, *Macromolecules* **2014**, *47*, 6836.
[20] V. Vijayakumar, Y. Zhong, V. Untilova, M. Bahri, L. Herrmann, L. Biniek, N. Leclerc, M. Brinkmann, *Adv. Energy Mater.* **2019**, *9*, 1900266.
[21] V. Vijayakumar, P. Durand, H. Zeng, V. Untilova, L. Herrmann, P. Algayer, N. Leclerc, M. Brinkmann, *J. Mater. Chem. C* **2020**, *8*, 16470.
[22] I. E. Jacobs, Y. Lin, Y. Huang, X. Ren, D. Simatos, C. Chen, D. Tjhe, M. Statz, L. Lai, P. A. Finn, W. G. Neal, G. D'Avino, V. Lemaur, S. Fratini, D. Beljonne, J. Strzalka, C. B. Nielsen, S. Barlow, S. R. Marder, I. McCulloch, H. Sirringhaus, *Adv. Mater.* **2022**, *34*, 2102988.

[23] D. M. DeLongchamp, R. J. Kline, E. K. Lin, D. A. Fischer, L. J. Richter, L. A. Lucas, M. Heeney, I. McCulloch, J. E. Northrup, *Adv. Mater.* **2007**, *19*, 833.
[24] S. Fratini, M. Nikolka, A. Salleo, G. Schweicher, H. Sirringhaus, *Nat. Mater.* **2020**, *19*, 491.
[25] B. Siegmund, A. Mischok, J. Benduhn, O. Zeika, S. Ullbrich, F. Nehm, M. Böhm, D. Spoltore, H. Fröb, C. Körner, K. Leo, K. Vandewal, *Nat. Commun.* **2017**, *8*, 15421.
[26] Z. Tang, Z. Ma, A. Sánchez-Díaz, S. Ullbrich, Y. Liu, B. Siegmund, A. Mischok, K. Leo, M. Campoy-Quiles, W. Li, K. Vandewal, *Adv. Mater.* **2017**, *29*, 1702184.
[27] A. C. Mayer, M. F. Toney, S. R. Scully, J. Rivnay, C. J. Brabec, M. Scharber, M. Koppe, M. Heeney, I. McCulloch, M. D. McGehee, *Adv. Funct. Mater.* **2009**, *19*, 1173.
[28] N. C. Miller, E. Cho, M. J. Junk, R. Gysel, C. Risko, D. Kim, S. Sweetnam, C. E. Miller, L. J. Richter, R. J. Kline, M. Heeney, I. McCulloch, A. Amassian, D. Acevedo-Feliz, C. Knox, M. R. Hansen, D. Dudenko, B. F. Chmelka, M. F. Toney, J. L. Brédas, M. D. McGehee, *Adv. Mater.* **2012**, *24*, 6071.
[29] N. C. Miller, E. Cho, R. Gysel, C. Risko, V. Coropceanu, C. E. Miller, S. Sweetnam, A. Sellinger, M. Heeney, I. McCulloch, J. L. Brédas, M. F. Toney, M. D. McGehee, *Adv. Energy Mater.* **2012**, *2*, 1208.
[30] J. Vanderspikken, Q. Liu, Z. Liu, T. Vandermeeren, T. Cardeynaels, S. Gielen, B. Van Mele, N. Van den Brande, B. Champagne, K. Vandewal, W. Maes, *Adv. Funct. Mater.* **2022**, *32*, 2108146.
[31] C. K. Lo, R. M. Wolfe, J. R. Reynolds, *Chem. Mater.* **2021**, *33*, 4842.
[32] J. Vanderspikken, P. Verstappen, W. Maes, *Macromolecules* **2024**, *57*, 7138.
[33] D. A. Warr, L. M. Perdigão, H. Pinfold, J. Blohm, D. Stringer, A. Leventis, H. Bronstein, A. Troisi, G. Costantini, *Sci. Adv.* **2018**, *4*, eaas9543.
[34] S. Moro, N. Siemons, O. Drury, D. A. Warr, T. A. Moriarty, L. M. Perdigão, D. Pearce, M. Moser, R. K. Hallani, J. Parker, I. McCulloch, J. M. Frost, J. Nelson, G. Costantini, *ACS Nano* **2022**, *16*, 21303.
[35] S. Moro, S. E. Spencer, D. W. Lester, F. Nübling, M. Sommer, G. Costantini, *ACS Nano* **2024**, *18*, 11655.
[36] D. M. DeLongchamp, R. J. Kline, Y. Jung, E. K. Lin, D. A. Fischer, D. J. Gundlach, S. K. Cotts, A. J. Moad, L. J. Richter, M. F. Toney, M. Heeney, I. McCulloch, *Macromolecules* **2008**, *41*, 5709.
[37] Z. Liu, J. Vanderspikken, K. Vandewal, W. Maes, B. Goderis, E. Nies, N. Van den Brande, B. Van Mele, manuscript submitted.
[38] E. Cho, C. Risko, D. Kim, R. Gysel, N. Cates, D. W. Breiby, M. D. McGehee, M. F. Toney, R. J. Kline, J.-L. Brédas, *J. Am. Chem. Soc.* **2012**, *134*, 6177.
[39] E. Buchaca-Domingo, K. Vandewal, Z. Fei, S. E. Watkins, F. H. Scholes, J. H. Bannock, J. C. de Mello, L. J. Richter, D. M. DeLongchamp, A. Amassian, M. Heeney, A. Salleo, N. Stingelin, *J. Am. Chem. Soc.* **2015**, *137*, 5256.
[40] K. Vandewal, K. Tvingstedt, A. Gadisa, O. Inganäs, J. V. Manca, *Nat. Mater.* **2009**, *8*, 904.